



# Efficient sampling of high-dimensional free energy landscapes using adaptive reinforced dynamics

Dongdong Wang<sup>1,2</sup>, Yanze Wang<sup>2,3</sup>, Junhan Chang<sup>2,3</sup>, Linfeng Zhang<sup>1,2</sup>✉, Han Wang<sup>4</sup>✉ and Weinan E.<sup>5,6,7</sup>

**Enhanced sampling methods such as metadynamics and umbrella sampling have become essential tools for exploring the configuration space of molecules and materials. At the same time, they have long faced a number of issues such as the inefficiency when dealing with a large number of collective variables (CVs) or systems with high free energy barriers. Here we show that, with clustering and adaptive tuning techniques, the reinforced dynamics (RiD) scheme can be used to efficiently explore the configuration space and free energy landscapes with a large number of CVs or systems with high free energy barriers. We illustrate this by studying various representative and challenging examples. First we demonstrate the efficiency of adaptive RiD compared with other methods and construct the nine-dimensional (9D) free energy landscape of a peptoid trimer, which has energy barriers of more than 8 kcal mol<sup>-1</sup>. We then study the folding of the protein chignolin using 18 CVs. In this case, both the folding and unfolding rates are observed to be 4.30 μs<sup>-1</sup>. Finally, we propose a protein structure refinement protocol based on RiD. This protocol allows us to efficiently employ more than 100 CVs for exploring the landscape of protein structures and it gives rise to an overall improvement of 14.6 units over the initial global distance test-high accuracy (GDT-HA) score.**

Over the past several decades, molecular dynamics (MD) has become an essential tool for modeling the structure and dynamics of biomolecules. At the same time, it has also been recognized that an essential difficulty with MD is the time-scale it can access because of the presence of a large number of (free) energy barriers in the (free) energy landscape of these biomolecules, because crossing such barriers is a rare event. Enhanced sampling methods have thus been proposed to accelerate sampling over the phase space. A useful idea is to add a biasing potential—a function of one or more collective variables (CVs) of the system—to the potential energy, so that the free energy barriers are reduced. Well-known examples of the application of such an idea include metadynamics (MetaD)<sup>1,2</sup> and umbrella sampling<sup>3</sup>. Both have become popular tools in molecular simulations. However, the effectiveness of these methods reduces greatly as the number of CVs increases. When the number of CVs is small, their choice is a critical issue for the accuracy of the methods. Yet, at the moment, there are still no systematic and reliable ways to choose CVs.

An important advance was temperature-accelerated MD (TAMD)<sup>4–6</sup>. This treats the CVs as dynamic variables, coupling them, adiabatically<sup>4</sup> or harmonically<sup>5,6</sup>, to the atomistic system by introducing an extended system and accelerating the sampling by using an artificially higher temperature for the variables. TAMD is a very effective tool for exploration. It allows for at least dozens of CVs to be used and has been successfully applied to large-scale systems<sup>7</sup>. With the aim of reconstructing the free energy surface (FES), Maragliano and colleagues<sup>8</sup> proposed the use of radial-basis functions, pre-dating work using neural networks. Whether these ideas can be used to accurately calculate the free energy of systems with a larger number of CVs, such as those reported here, is a non-trivial issue that remains to be addressed.

Recently, some efforts have been made to deal with larger numbers of CVs under the MetaD framework. Bias-exchange metadynamics (BEMetaD)<sup>9</sup> is proposed to simulate multiple replicas at the same temperature, and each replica is biased with a different set of CVs. Using the replica exchange idea, BEMetaD is able to construct FESs in the high-dimensional CV space. Parallel bias metadynamics (PBMetaD)<sup>10,11</sup> constructs a high-dimensional bias potential through the weighted direct product of low-dimensional ones, and boosts the sampling with only one replica. These methods can be implemented under the well-tempered MetaD scheme. Both BEMetaD and PBMetaD assume that the biasing potential is a direct product, so they are effective only when the FES has a similar structure, which is not necessarily true for general high-dimensional problems.

Recent advances in machine learning offer powerful tools for approximating high-dimensional functions. Several attempts have been made in this regard<sup>12–20</sup>. These approaches represent the FES by high-dimensional approximators like kernel functions or deep neural networks (DNNs). What differentiates the different approaches is how one optimizes the parameters of the approximators and how the approximators are used on-the-fly to facilitate sampling. The Gaussian process regression is used to reconstruct the FES<sup>12</sup> and to enhance the sampling of the system<sup>13</sup>. DNNs trained by stochastic optimization techniques are proposed to represent the FESs<sup>14</sup>. The efficiency of sampling is enhanced by biasing the system with DNNs trained from density estimations<sup>16</sup> or from mean forces<sup>17</sup>. Sultan and colleagues proposed nonlinear latent embedding for obtaining the latent CVs<sup>18</sup>. The neural network-based variationally enhanced sampling (VES) approach<sup>19</sup> minimizes the Kullback–Leibler divergence between the distribution of the CVs and a target distribution<sup>21,22</sup>. The performance of these approximators has also

<sup>1</sup>Program in Applied and Computational Mathematics, Princeton University, Princeton, NJ, USA. <sup>2</sup>DP Technology, Beijing, People's Republic of China.

<sup>3</sup>College of Chemistry and Molecular Engineering, Peking University, Beijing, People's Republic of China. <sup>4</sup>Laboratory of Computational Physics, Institute of Applied Physics and Computational Mathematics, Beijing, People's Republic of China. <sup>5</sup>School of Mathematical Sciences, Peking University, Beijing, People's Republic of China. <sup>6</sup>Department of Mathematics and Program in Applied and Computational Mathematics, Princeton University, Princeton, NJ, USA.

<sup>7</sup>Beijing Institute of Big Data Research, Beijing, People's Republic of China. ✉e-mail: [linfeng.zhang.zlf@gmail.com](mailto:linfeng.zhang.zlf@gmail.com); [wang\\_han@iapcm.ac.cn](mailto:wang_han@iapcm.ac.cn)

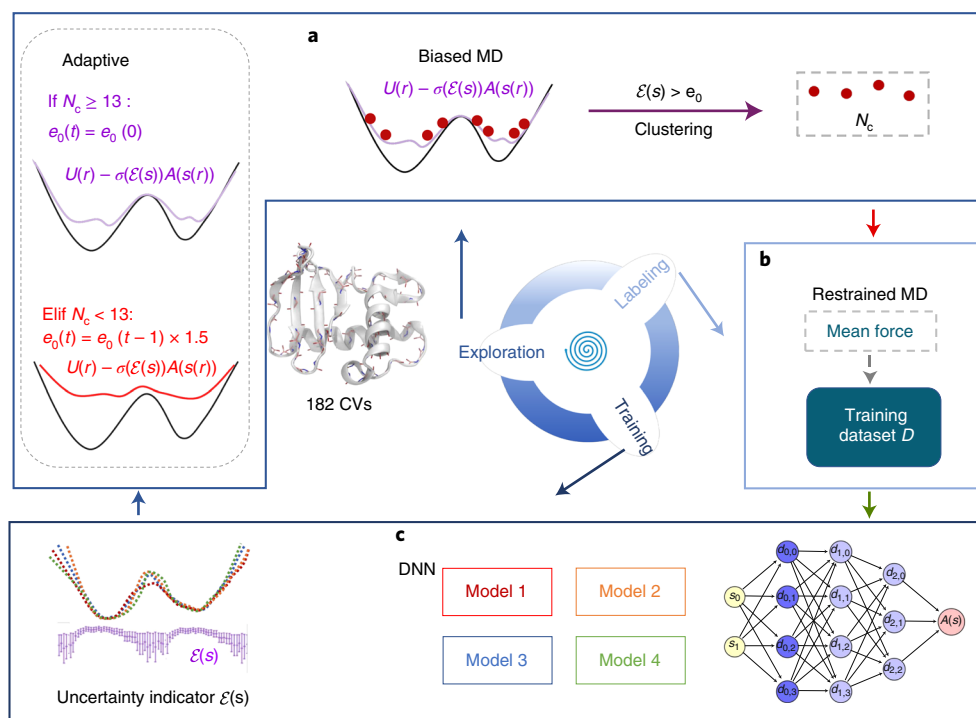


**Fig. 1 | The workflow of adaptive RiD.** Adaptive RiD iteratively and automatically promotes exploration, labeling and training steps. **a**, Biased MD is used in the exploration step, and the visited CV values with the uncertainty indicators  $\mathcal{E}(s)$  larger than a certain level  $e_0$  are proposed for labeling. The proposed CVs are then clustered into  $N_c$  clusters and one set of CV values is randomly selected from each cluster for labeling. An adaptive strategy is used at each iteration by changing the uncertainty levels according to the number of clusters  $N_c$ . In detail, if  $N_c$  is less than 13, then the level  $e_0$  is multiplied by 1.5 and  $e_t = e_0 + 1$ , otherwise the same levels as the initial values are used (panel outlined by a gray dashed line). **b**, The mean forces evaluated by the restrained MD simulation are used as labels to train the DNN models. **c**, Four DNN models are trained by using different random initial parameters and the uncertainty indicator  $\mathcal{E}(s)$  is defined as the standard deviation of the force predictions from this ensemble of DNN models.

been studied by Cendagorta and colleagues<sup>23</sup>. Their results show that the kernel method typically requires a larger memory and its performance deteriorates as the number of CVs increases, whereas the neural network models are more robust and accurate.

The starting point of the present work is the reinforced dynamics (RiD) scheme introduced in ref. <sup>15</sup>. RiD uses an uncertainty indicator to decide where to bias the MD simulation and at which values of the CVs one should calculate the mean force. The accumulated CVs and mean forces are used for training and refining the DNN parameters. RiD has been shown to be successful in exploring spaces with no more than 20 CVs, but its efficiency deteriorates quickly with more CVs. Indeed, it has been observed becoming trapped in the deep local minima in higher-dimensional systems. This difficulty is caused by two factors. First, the probability of visiting the neighborhood of a local minimum in a high-dimensional CV space is much lower than that in lower-dimensional cases. Thus, a random batch of RiD samples is not enough for reconstructing the landscape near the local minimum of a high-dimensional FES. Second, the biasing mechanism is too rigid for exploration and, in particular, for escaping from deep local minima.

Despite all these efforts, we are still unable to tackle challenging tasks such as protein structure refinement, in which MD simulations are used to refine the decoys predicted by data-driven methods. Such a task usually requires repetition of the unfolding and refolding processes, which requires very large computational times because of the kinetic barriers. Enhanced sampling methods such as replica exchange MD (REMD) simulation<sup>24</sup> and metadynamics could, in principle, be used to overcome such barriers. In practice, however, REMD is very expensive and, with metadynamics, it is unclear how to choose a low-dimensional CV space even for small

proteins with dozens of residues, in the absence of knowledge of the native structure. If one chooses all the dihedral angles (twice the number of residues) as the CVs, then the approaches discussed above may, in principle, be applied. However, in practice, to the best of our knowledge, these methods have never been reported to be able to handle problems with more than 100 CVs, so their effectiveness in solving the protein structure refinement problem remains unknown.

In this Article we propose an adaptive version of the RiD scheme that has the potential to overcome the difficulties with RiD, and we demonstrate its effectiveness on several challenging examples. The novelty of the adaptive RiD rests in two aspects: (1) a clustering algorithm is applied to the configurations selected for labeling to reduce the number of configurations needed to represent the unexplored configuration space and (2) the uncertainty indicator and the bias are adaptively and automatically tuned by using the same clustering argument that quantifies the diversity of the explored configurations. This helps to encourage RiD to escape from the deep local minima. In addition, adaptive RiD supports a multi-walker scheme, which allows us to make full use of parallel computational platforms.

## Results

The adaptive RiD method runs in iterations and each iteration consists of three steps (Fig. 1): exploration, labeling and training. In the exploration step, the sampling of the configuration space is enhanced by a biasing force defined in the CV space. The biasing force is switched on (or off) according to the value of an uncertainty indicator that is defined as the standard deviation of the force predictions from an ensemble of DNN models. The explored

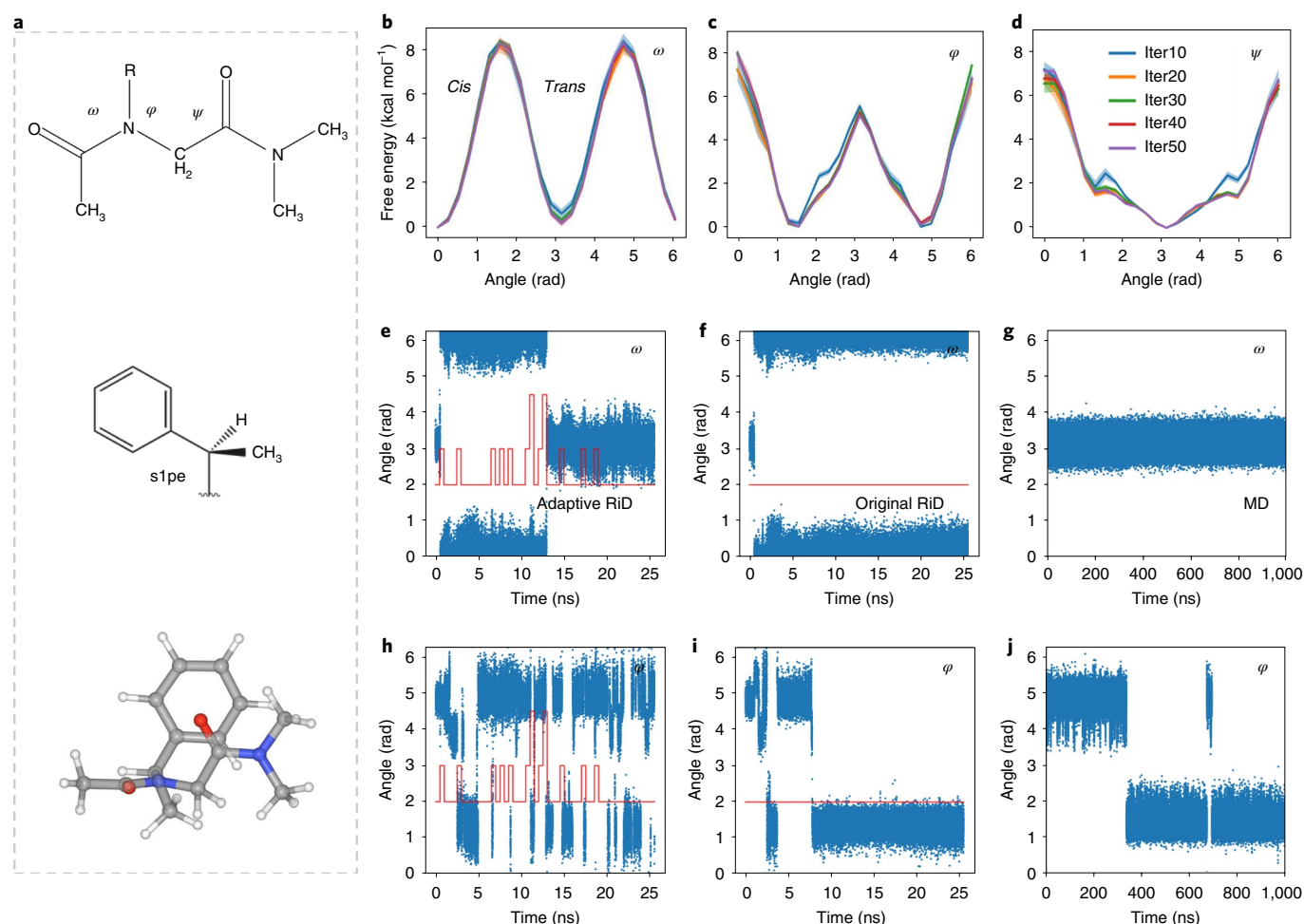


**Fig. 2 | The accuracy and efficiency of adaptive RiD.** **a**, Backbone plot, side-chain plot and 3D structure of the peptoid s1pe. The 3D structure is shown in ball-and-stick representation and colored by atom: nitrogen (blue), oxygen (red), hydrogen (white) and carbon (gray). **b–d**, Free energy curve of each CV of the peptoid s1pe ( $\omega$  (**b**),  $\phi$  (**c**) and  $\psi$  (**d**)) at different iterations (10th, 20th, 30th, 40th and 50th). **e–j**, The transitions of angles for the first walker of an adaptive RiD simulation (**e,h**), the first walker of an original RiD simulation (**f,i**) and a brute-force MD simulation (**g,j**) as a function of the simulation time. Blue dots represent the torsion angles of  $\omega$  (**e–g**) and  $\phi$  (**h–j**) of s1pe. The values of uncertainty level  $e_0$  in adaptive RiD and original RiD simulations are shown as red lines.

configurations are selected first according to the uncertainty indicator, then by a clustering argument, so that a diversified subset of the sampled configurations with large model prediction error is selected. In the labeling step, we calculate the mean force of every selected configuration as its label. In the training step, we train an ensemble of DNN models with random and independent parameter initializations. More details on the adaptive RiD method are provided in the Methods.

Four representative systems are used here to illustrate the performance of adaptive RiD. First we use the peptoid system to compare adaptive RiD with its original version. We then move on to a more complex situation, the peptoid trimer with relatively large energy barriers, for which we construct a nine-dimensional (9D) free energy landscape and compare adaptive RiD with other methods. Next, we study a classical protein system, chignolin. Using the 18 backbone dihedral angles as the CVs, we can use adaptive RiD to efficiently sample the folding and unfolding states of chignolin. Finally, we use adaptive RiD to help refine the protein structures of three targets in CASP13 using more than 100 CVs.

**Peptoid.** Peptoids are a family of synthetic oligomers composed of protein-like, poly-glycine backbones with side chains (R) attached to the amide nitrogen atoms rather than their  $\alpha$ -carbons<sup>25,26</sup> (Fig. 2a).

Recently, peptoids have received substantial interest due to their resemblance to peptides, with applications such as bioactive peptide mimics<sup>27</sup> and targeted binders<sup>28,29</sup>. Despite a great amount of effort<sup>30–33</sup>, efficient sampling of peptoid configurations remains challenging and is far from being routine due to the high dimensionality and large energy barriers in the space of torsion angles.

In this Article, we first consider a simple peptoid, s-(1)-phenylethyl (s1pe), obtained from Weiser's work<sup>33</sup>. The adaptive RiD simulation was conducted for 51 iterations, corresponding to a 25.5-ns biased MD simulation for each walker (see Methods for details). The calculated FES is fully converged within 40 iterations, as shown in Fig. 2b–d. The error of the FES, estimated from the maximal standard deviation of four DNN models, is 0.31 kcal mol<sup>−1</sup>. Remarkably, the free energy difference between the *trans* ( $\omega \approx 180^\circ$ ) and *cis* ( $\omega \approx 0^\circ$ ) conformations is  $0.18 \pm 0.07$  kcal mol<sup>−1</sup>, which agrees quite well with experiment (0.14 kcal mol<sup>−1</sup>)<sup>34</sup>. We show that the FES is consistent with previous simulation results<sup>33</sup> (Supplementary Fig. 1) and with that calculated by the REMD method (Supplementary Fig. 2).

We demonstrate the improvement of adaptive RiD over the original RiD and brute-force MD in terms of sampling efficiency by studying the transition events. As shown in Fig. 2g,j, a 1- $\mu$ s-long brute-force MD simulation exhibits very few transitions of the

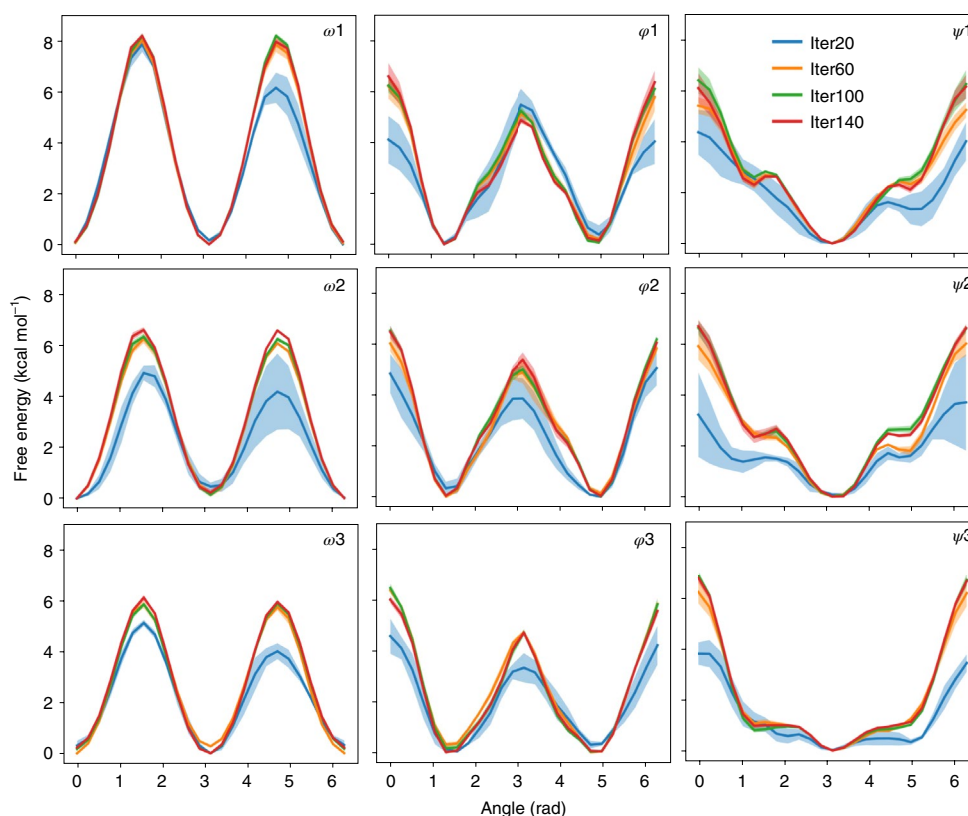


**Fig. 3 | Free energy curves of the peptoid trimer (s1pe)<sub>3</sub>.** Free energy curve of each CV of the peptoid trimer (s1pe)<sub>3</sub>. The free energy curves derived from different iterations (20th, 60th, 100th and 140th) are drawn to assess the convergence of adaptive RiD. Error bars (shading) are calculated based on four DNN models.

torsion angles  $\omega$  and  $\phi$ . Transitions take place in a 25.5-ns-long original RiD simulation (Fig. 2f,i), but less frequently than those in an adaptive RiD simulation of the same length (Supplementary Table 1). The number of explored transition states ( $\omega \in [3\pi/8, 5\pi/8] \cup [11\pi/8, 13\pi/8]$ ) is 725 and 266 for adaptive and original RiD, respectively. No transition states can be seen from the REMD simulations (Supplementary Fig. 2). In conclusion, adaptively changing the uncertainty level  $e_0$  (red lines, Fig. 2e–j; for a definition see Methods) helps to accelerate the exploration of conformation space.

We also consider a more complex system, the peptoid trimer (s1pe)<sub>3</sub>, which exhibits high free energy barriers in the space of nine torsion angles  $\omega_1, \phi_1, \psi_1, \omega_2, \phi_2, \psi_2, \omega_3, \phi_3$  and  $\psi_3$ . A previous study showed that it is hard to observe transitions of torsion angles  $\omega$  and  $\phi$  in simulations with explicit solvent<sup>33</sup>. In our simulation, 12 walkers are used and each lasts for 140 iterations. The biased MD simulation in each iteration lasts 2 ns (see Methods for details). As can be seen from Supplementary Table 2, we observed tens to hundreds of transitions of the six torsion angles  $\omega_1, \omega_2, \omega_3, \phi_1, \phi_2$  and  $\phi_3$ , much more than observed in a previous work<sup>33</sup>, which performed an 85-ns brute-force MD simulation at 950 K. The overall trend of the transition frequency at different angles is qualitatively consistent with the results of previous MD simulations at high temperature<sup>33</sup>.

We use a Markov chain Monte Carlo (MCMC) scheme to project the FES on fewer CVs (see Methods for details). Figure 3 shows an energy barrier of more than 8 kcal mol<sup>−1</sup> in  $\omega_1$ . The free energy differences between metastable states can be estimated fairly accurately at an early stage of the adaptive RiD simulation (20th iteration). In fact, the FES has almost converged after 60 iterations (~1,440 ns). Note that the FES in the space of  $\psi_3$  is quite flat over a large region. This indicates that the carboxy termini ( $\phi_3, \psi_3$ ) are quite flexible, confirming the conclusions of a previous study<sup>33</sup> using high-temperature simulations.

As a comparison, we calculated the FES of the peptoid trimer using REMD simulations (see Methods for more details and discussion). The FES calculated by REMD is sensitive to the setting of the temperature range. Even with the optimal temperature range, the transition states of the  $\omega$  and  $\phi$  angles are not properly sampled by REMD, so the free energy profile is hard to converge at the transition states. This difficulty can be avoided by using adaptive RiD. BEMetaD and PBMetaD simulations were also conducted as another comparison. The same set of CVs and nine replicas were used under different conditions (detailed in the Methods). The free energy curve of each angle essentially converges after 160 ns for each replica (Supplementary Fig. 3), accumulating to a total of 1,440 ns of simulation time, with the same time as adaptive RiD. The free energy curves of BEMetaD, PBMetaD, adaptive RiD and REMD are in good agreement (Supplementary Fig. 4), and their errors with respect to the best converged REMD (300–680 K, 400 ns each replica) are similar (Supplementary Table 3). Overall, adaptive RiD has efficiency and accuracy comparable to those of BEMetaD and PBMetaD.0

**Chignolin.** The folding of small proteins serves as a good benchmark for first-principles-based methodologies. Here we investigate the artificial protein chignolin, which has a  $\beta$ -hairpin structure (with ten residues), as an example. There are extensive experimental<sup>35</sup> and simulation studies<sup>22,36–39</sup> for this system. Using the Anton computer, an MD simulation lasting longer than 100  $\mu$ s has been conducted<sup>36</sup> and folding and unfolding times of ~0.6  $\mu$ s and 2.2  $\mu$ s, respectively, have been observed.

Adaptive RiD uses 18 backbone dihedral angles as the CVs with 12 walkers in parallel. The initial configurations are randomly extended conformations and 31 iterations are conducted. In each iteration, a 5-ns biased MD simulation is performed for each walker (see Methods for details). As shown in Fig. 4a,b, the folding



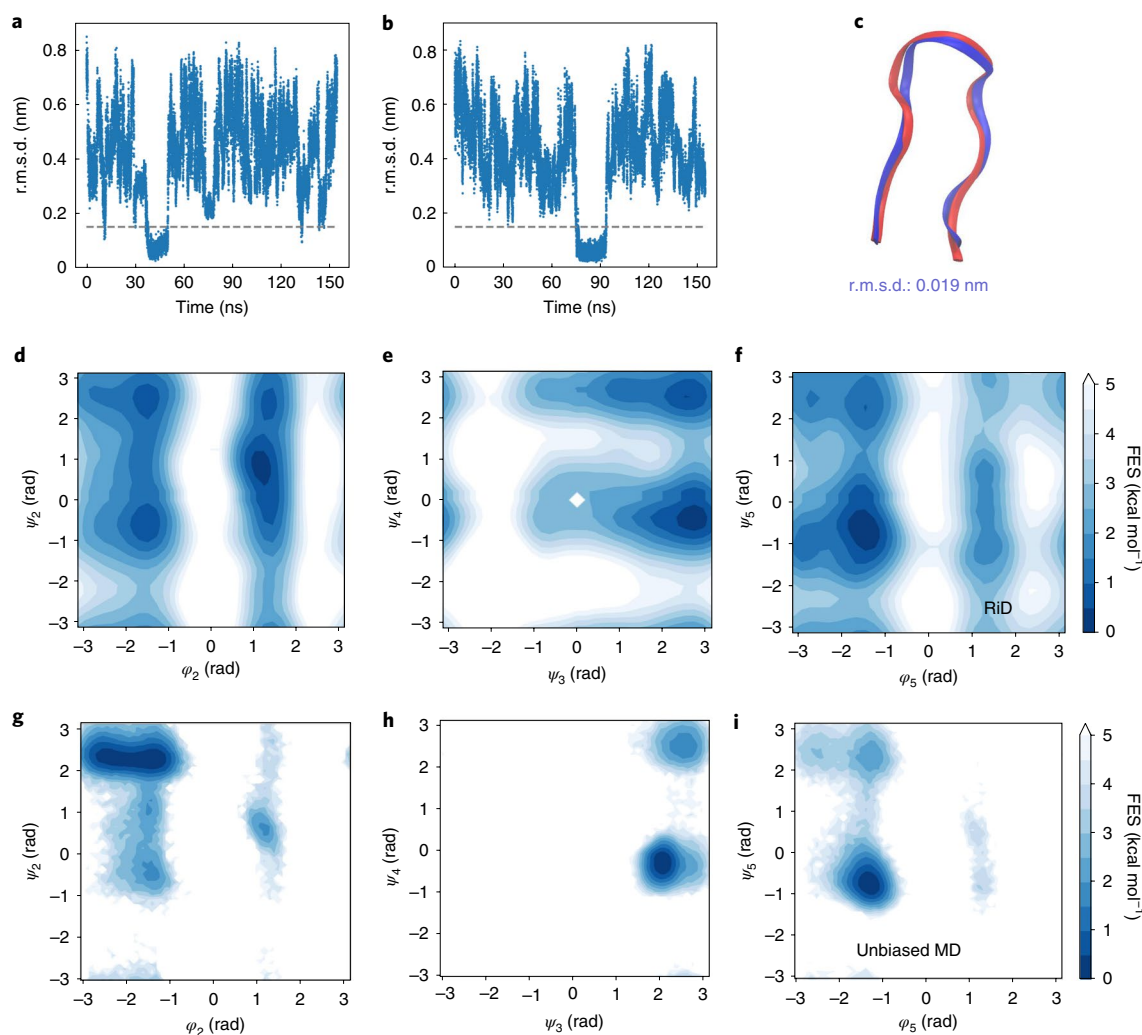


**Fig. 4 | Folding and unfolding of the protein chignolin. a,b**, Time series of the C $\alpha$  r.m.s.d. from the reference structure for chignolin for two walkers in adaptive RiD. Structures with r.m.s.d. of <0.15 nm (gray dashed line) are defined as folded states. **c**, The folded structure obtained from adaptive RiD (blue) superimposed on the reference structure (red). The C $\alpha$  r.m.s.d. is 0.019 nm. **d–f**, FESs (kcal mol $^{-1}$ ) of  $\varphi_2$  and  $\psi_2$  (**d**),  $\psi_3$  and  $\psi_4$  (**e**) and  $\varphi_5$  and  $\psi_5$  (**f**) from adaptive RiD. **g–i**, The FESs corresponding to **d** (**g**), **e** (**h**) and **f** (**i**) obtained from a 100  $\mu$ s unbiased MD trajectory from the work of Lindorff-Larsen and others<sup>36</sup>.

and unfolding events are observed within a few iterations. The minimum C $\alpha$  root-mean-square deviation (r.m.s.d.) is 0.019 nm (Fig. 4b,c). Both the folding and unfolding rates are observed to be 4.30  $\mu$ s $^{-1}$ . Therefore, adaptive RiD efficiently samples the folding and unfolding events of chignolin without prior knowledge on the native state, unlike the VES scheme<sup>22</sup>, which needs a target distribution to lead the sampling. BEMetaD and PBMetaD simulations were also conducted to compare with adaptive RiD. The same set of CVs was used and different working parameters were considered (see Methods for details). The folding and unfolding rates are reported in Supplementary Table 5. Overall, the adaptive RiD and all variants of MetaD successfully fold chignolin, but only the adaptive RiD and PBMetaD can escape from the native state. This implies that adaptive RiD and PBMetaD are more suitable for larger proteins that have deep metastable states on the free energy landscape.

In Fig. 4 we compare the FES calculated by adaptive RiD (Fig. 4d–f) with a 100- $\mu$ s unbiased MD trajectory (Fig. 4g–i). We find qualitative agreement between the two results, and adaptive RiD samples a broader region in the conformation space using a much shorter exploration time (1.8  $\mu$ s). The result also agrees well with those obtained by the VES scheme in a previous study<sup>22</sup>.

**Protein structure refinement.** In the past few years, substantial progress has been made on the protein folding problem. Of particular importance is the reported remarkable achievement of AlphaFold2<sup>40</sup>. However, for 47% of all targets or 37% of those with fewer than 100 residues, the structures predicted by AlphaFold2 in CASP14 have global distance test–high accuracy (GDT-HA)<sup>41</sup> scores of less than 75. GDT-HA scores range from 0 to 100, and a higher score means a higher similarity between the predicted and native structures. For these structures, an additional structure refinement procedure might generate better predictions. Several refinement protocols have been reported in the literature<sup>42–47</sup>, including those based on MD simulations<sup>43,44</sup>. In the refinement category of the CASP13 competition, in which the goal is to generate a better predicted structure using the given decoys as starting points, FEIGLAB, using MD simulations, achieved the best results, with an average improvement in the GDT-HA scores of ~3.99 units. However, as the authors noted, sufficient sampling remains challenging for some proteins because of the kinetic barriers<sup>47</sup>.

Here we choose three CASP13 targets—R0974s1, R0986s1 and R1002-D2—which were analyzed in detail in the work of Heo and colleagues<sup>47</sup>. We use eight walkers and perform 16 iterations. Each

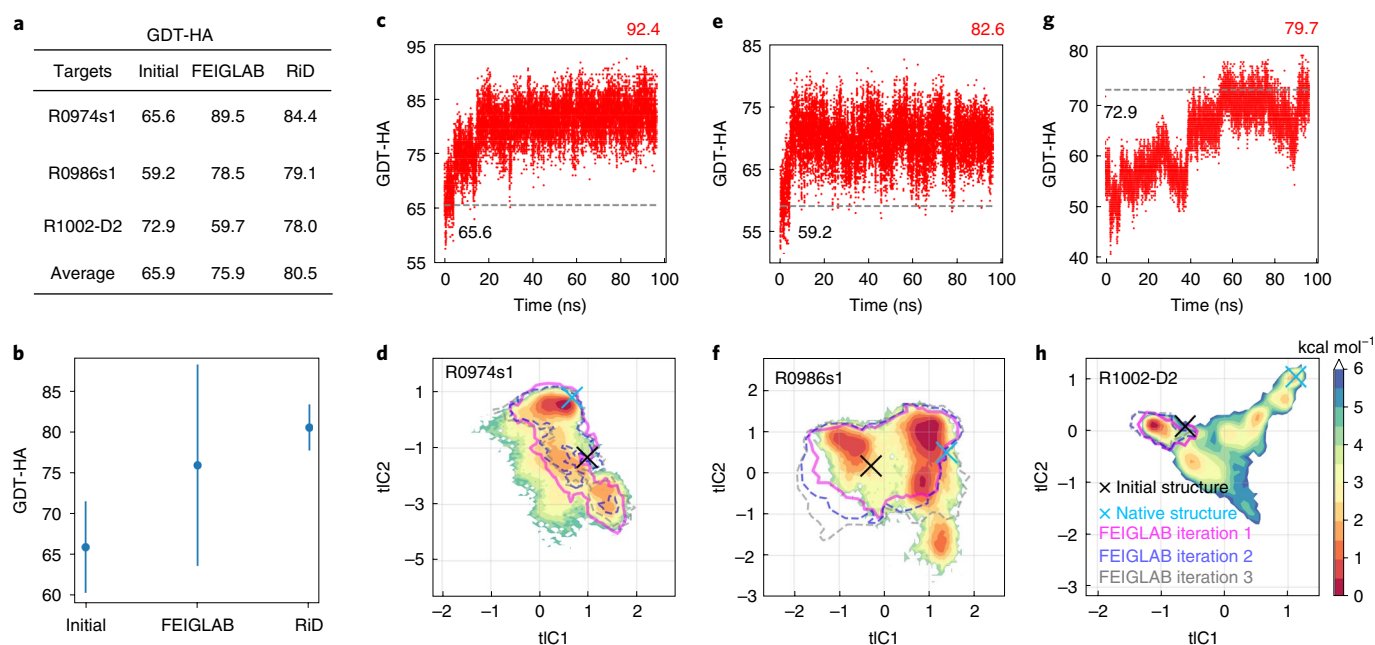


**Fig. 5 | Protein structure refinement of three targets: R0974s1, R0986s1 and R1002-D2. a,b**, The values (a) and plot (b) of the GDT-HA scores of the initial structures, the refined structures of FEIGLAB and the refined structures of adaptive RiD. The error bars in b represent the standard deviations of these three targets. **c,e,g**, Time series of the GDT-HA score of one representative trajectory for each target: R0974s1 (c), R0986s1 (e) and R1002-D2 (g). **d,f,h**, Density plots of the two tIC coordinates used in the MSM analysis in Heo's work<sup>47</sup>, along the adaptive RiD trajectories of R0974s1 (d), R0986s1 (f) and R1002-D2 (h). The explored regions in ref. <sup>47</sup> for these targets are drawn as a magenta line (iteration 1), blue dashed line (iteration 2) and gray dashed line (iteration 3), respectively.

iteration lasts 6 ns, so a total of 96 ns of biased MD simulation is conducted for each walker. The 136, 182 and 116 dihedral angles of these three targets are used as CVs, respectively. In addition, to prevent transitions to the unfolded states, we apply a flat-bottomed harmonic restraint potential to each C $\alpha$  atom<sup>47</sup> (see Methods for details). The refined structure is constructed by averaging 200 structures with the lowest RWplus values<sup>48</sup> along the adaptive RiD trajectories. The effectiveness of adaptive RiD in improving the GDT-HA score is reported and compared with the results of FEIGLAB in Fig. 5a,b. The three targets have initial GDT-HA scores of 65.6, 59.2 and 72.9, respectively, and are all refined to beyond 78.0 under the adaptive RiD scheme. Special attention is drawn to R1002-D2, the score of which is improved to 78.0 after the refinement, but is notably worse than the score obtained by FEIGLAB<sup>47</sup>. The average improvement in GDT-HA score is 14.6 units. The standard deviation is 2.8. This low value shows the robustness of adaptive RiD.

To see how the protein structures are explored by adaptive RiD, we calculated the GDT-HA scores along the adaptive RiD trajectories and found the best sampled structures with GDT-HA scores of 92.4, 82.6 and 79.7, respectively (Fig. 5c,e,g). Note that the structures with high scores are quickly reached within 20 ns in the cases of R0974s1 and R0986s1. By contrast, for R1002-D2, the GDT-HA score quickly drops at the beginning of the simulation, then transitions to a better score after more than 40 ns. To further compare the conformational space explored by adaptive RiD with that sampled by FEIGLAB, we projected the trajectories onto the two time-structure independent component (tIC) coordinates used in the Markov state model (MSM) analysis of the FEIGLAB study (Fig. 5d,f,h). We find that, compared with the 2- $\mu$ s-long brute-force simulations in the FEIGLAB sampling protocols, comparable conformation spaces are sampled by the 768-ns-long adaptive RiD simulations of R0974s1 and R0986s1, and a much larger conformation space is sampled in the case of R1002-D2. Indeed, for R1002-D2, the FEIGLAB

simulation only found one metastable state out of the three states that were investigated in their MSM study, but adaptive RiD finds all three, including the native state.

To see how adaptive RiD finds the native state of R1002-D2 from a conformational change perspective, we performed a detailed analysis (Fig. 6). According to Fig. 6a–c, it is clear that the initial structure has a high similarity to the native structure, but, during the adaptive RiD simulation, the walker first goes to a metastable state that is distant from both the initial structure and the native structure, and it then falls into the basin of the native structure. In detail, as shown by the red arrow in Fig. 6d, there is a register-shift error of  $\sim 0.57$  nm in the N-terminal  $\beta$ -strand of the initial structure. Then, during the simulation, the hydrogen bonds between the  $\beta$ -strands break at first and lead to a large conformational change with more than 0.4 nm in r.m.s.d. compared with both the initial model and the native structure (Fig. 6a,b,e). It is only after this large conformational change that the correct  $\beta$ -strand is seen and a more accurate structure with r.m.s.d. of  $\sim 0.11$  nm is found (Fig. 6f). We thus attribute the success of adaptive RiD to its ability to cross over the high free energy barrier along the transition path to the native state. The same barrier forbids the FEIGLAB protocol from discovering the transition path.

## Discussion

With the ability to handle a large number of CVs, RiD is very powerful in exploring the configuration space of atomistic systems. The added feature of adaptively changing the bias helps to facilitate the escape from metastable states and crossing large energy barriers. Moreover, adaptive RiD supports a multi-walker scheme, and it is very much suited for parallelization. It also opens up new possibilities, such as free energy calculation of the binding of peptides or intrinsically disordered proteins to proteins, the study of the ensemble nature of allostery, and structure optimization in materials science.

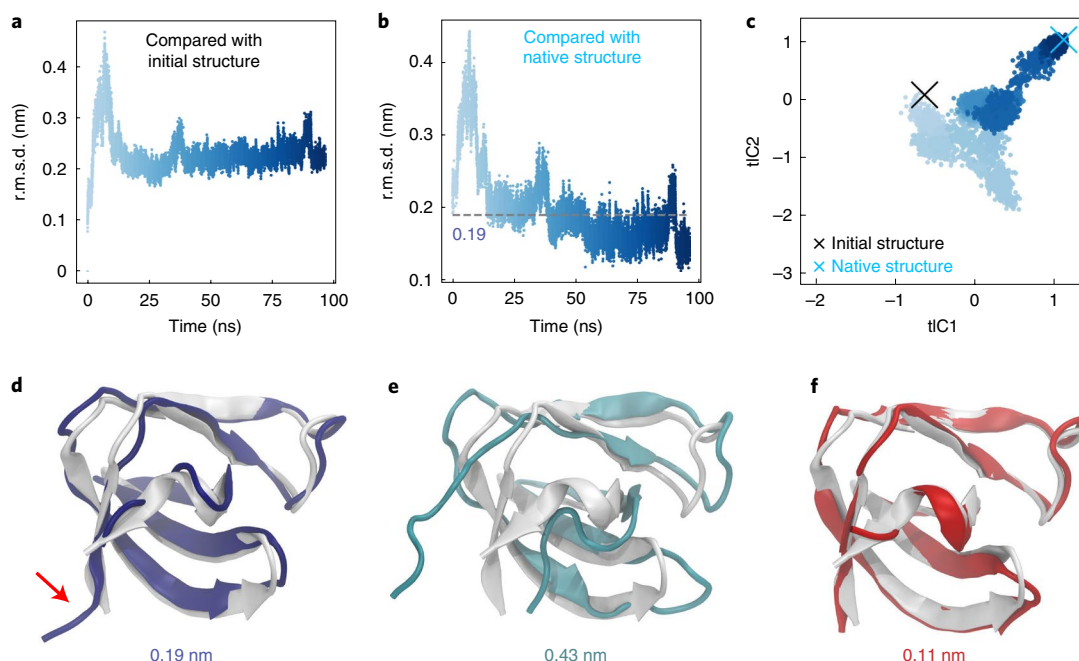


**Fig. 6 | Detailed analysis of the target R1002-D2. a,b,** Time series of the r.m.s.d. between the structures along a representative trajectory and the initial structure (**a**) or native structure (**b**). **c,** One representative adaptive RiD trajectory projected on the two tIC coordinates. Each circle represents one snapshot and is colored at different times from light blue to dark blue in **a–c**. **d–f,** The native structure (white) superposed on the initial structure (**d**, blue), the unfolded structure (**e**, cyan) and refined structure (**f**, red), respectively. R.m.s.d. values for the initial structure, unfolded structure and refined structure compared with the native structure are shown in **d–f**, respectively.

Several improvements may further enhance the performance of adaptive RiD. For example, for *ab initio* folding of large proteins, the space of dihedral angles might be too large, and a better set of CVs might be needed. For the protein refinement task, with the help of quality assessment<sup>49</sup> of protein tertiary structures, we may choose to include only the dihedral angles in the residues with poor quality as the CVs, to reduce computational cost. We leave these possibilities to the future.

## Methods

**The adaptive RiD method.** We considered  $N$  atoms in a canonical ensemble, the potential energy of which is denoted by  $U(r)$ ,  $r = (r_1, \dots, r_N)$ . Given  $M$  predefined CVs, denoted by  $s$ , the free energy defined on the CV space is denoted by  $\mathcal{A}(s)$ . A DNN, denoted by  $\mathcal{A}(s, w)$ , is used to model the free energy, with  $w$  being the network parameters. For a given set of CV values, the mean forces  $F(s) = -\nabla_s \mathcal{A}(s)$  are evaluated by restrained MD simulations<sup>8</sup> by adding a harmonic potential between the target and the instantaneous CVs, and  $F$  is estimated by the averaged restraining force. The mean forces  $F(s)$  are then used as labels to train the DNN models (Fig. 1b,c).

To guarantee the accuracy of the neural network approximation of  $\mathcal{A}$ , one should have an adequate training dataset  $D$ . How to efficiently explore the CV space and how to select the explored data points for labeling are the key components of RiD. The key quantity that helps for both purposes is the uncertainty indicator  $\mathcal{E}(s)$ , which is defined as the standard deviation of the force predictions from a small ensemble of DNN models with the same network architecture but trained with different randomly initialized parameters. This ensemble of models typically gives rise to consistent predictions of the mean force in regions well covered by  $D$  and scattered predictions in regions poorly covered by  $D$  (Fig. 1c).

As shown in Fig. 1a, one biases the potential energy  $U(r)$  by the current approximation of the FES, so that the system is encouraged to escape free energy minima and explore a broader region in the CV space. Because the approximation of FES is of high (or low) accuracy in regions that have been (or have not been) adequately explored, the bias is switched on (or off) according to the value of the uncertainty indicator  $\mathcal{E}(s(r))$ :

$$\tilde{f}_i(r) = -\nabla_{r_i} U(r) + \sigma(\mathcal{E}(s(r))) \langle \nabla_{r_i} \mathcal{A}(s(r), w) \rangle, \quad (1)$$

where the biasing potential  $-\langle \mathcal{A}(s(r), w) \rangle$  is the mean value of the predictions of the predefined ensemble of DNN models and  $\sigma(\cdot)$  is a fixed switching function that varies smoothly between two uncertainty levels  $e_0$  and  $e_1$ . When the uncertainty

value is smaller than  $e_0$ , the accuracy of the FES approximation is adequate and the bias is switched on with  $\sigma(\mathcal{E}) = 1$ . When the uncertainty value is larger than  $e_1$ , the bias is switched off ( $\sigma(\mathcal{E}) = 0$ ) and the dynamics of the system falls back to that governed by the original potential energy  $U(r)$ . The switching function is defined by

$$\sigma(\epsilon) = \begin{cases} 1, & \epsilon < e_0 \\ \frac{1}{2} + \frac{1}{2} \cos(\pi \frac{\epsilon - e_0}{e_1 - e_0}), & e_0 < \epsilon < e_1 \\ 0, & \epsilon > e_1 \end{cases} \quad (2)$$

During the exploration, the visited CV values are tested by the uncertainty indicator and proposed for labeling if the uncertainty is relatively large, in other words  $\mathcal{E}(s) > e_0$  (Fig. 1a). The proposed CVs are first clustered by the agglomerative clustering algorithm, and one CV values is randomly selected from each cluster for labeling. This reduces the number of samples in the CV space needed for labeling, without affecting the representativeness of these samples. This CV selection procedure is applied after the exploration step in every adaptive RiD iteration. Finally, the selected CV values and the associated labels are added to the training dataset  $D$ , from which a new ensemble of DNN models are trained. The new iteration is started over with the updated model ensemble.

The uncertainty levels  $e_0$  and  $e_1$  are two crucial parameters in the RiD method. A large level would encourage exploration at the cost of lowering the accuracy of the FES approximation. A small level gives more accurate approximation of the local FES, but the system is easily trapped by deep energy wells. Here we adaptively change the uncertainty levels at each iteration. In detail, the explored configurations are clustered by the agglomerative clustering algorithm. If the number of clusters is less than some fixed value  $K_0$  ( $K_0 = 13$  for this work), then the level  $e_0$  is multiplied by 1.5 and  $e_1 = e_0 + 1$ , otherwise the same levels as the initial values are used. If  $e_0$  is more than eight times larger than its initial value, then both levels are reset to their initial values (Fig. 1a, gray panel). We refer to this as adaptive RiD. A comparison of the efficiencies of the original RiD and adaptive RiD is given in the following sections.

**Simulation protocol.** We used the GROMACS/2019.2 software package<sup>50</sup> with a modified version of the PLUMED/2.5.2 plugin<sup>51</sup> to conduct all MD simulations. The PLUMED package was modified to compute the DNN biasing force (equation (1)). We thus first minimize the energy of proteins using the steepest descent algorithm. The added solvent is then equilibrated with position restraints on the heavy atoms of the protein. The temperature is maintained using the V-rescale method<sup>52</sup> with a relaxation time of 0.2 ps. A Parrinello–Rahman barostat<sup>53</sup> is used to keep the pressure at 1 bar with a time constant of 1.5 ps. The cutoffs of electrostatic interactions and van der Waals interactions are both set to 1 nm, and the particle



mesh Ewald method<sup>54</sup> is used to treat electrostatic interactions. All bonds involving hydrogen atoms are constrained by the LINCS algorithms<sup>55</sup>.

**Peptoid.** To assess the accuracy and efficiency of adaptive RiD, we first studied one example system, the peptoid with side chain *s*-(1-phenylethyl) (s1pe), which was obtained from Weiser's work<sup>33</sup>. For this, the molecules are solvated in 2.9 nm × 2.9 nm × 2.9 nm dodecahedron boxes with 546 water molecules. The final systems contain 1,676 atoms. All simulations are carried out with the CHARMM general force field (CGenFF) parameters developed for peptoids<sup>33</sup> and the TIP3P water model<sup>56</sup> for the explicit solvent. The temperature is maintained at 300 K. After a conventional 1,000-ns MD simulation is conducted, 12 conformations are randomly selected from the trajectory for the initial configurations of adaptive RiD. Three torsion angles,  $\omega$  ( $C_\alpha$ , C, N,  $C_\beta$ ),  $\phi$  (C, N,  $C_\alpha$ , C) and  $\psi$  (N,  $C_\alpha$ , C, N), are chosen as CVs, that is,  $s = (\omega, \phi, \psi)$ . The preprocessing operator is taken as  $P(\omega, \phi, \psi) = (\cos(\omega), \sin(\omega), \cos(\phi), \sin(\phi), \cos(\psi), \sin(\psi))$ , so the periodic condition of the FES is guaranteed. Twelve walkers with different conformations of adaptive RiD are conducted using 500-ps biased MD simulations. The CV values along the MD trajectories are computed and recorded every 0.5 ps. We assume no prior information regarding the FES, so brute-force simulations are performed for the 0th iteration step (we count the iterations from 0). In each iteration, the recorded CV values in the region with high uncertainty are clustered using the agglomerative clustering algorithm with a distance threshold. The distance threshold is chosen such that, for a conventional MD simulation, ~15 clusters are formed. One CV value from each cluster is added to the training dataset  $D$ . Restrained MD simulations with spring constant 500 kJ mol<sup>-1</sup> rad<sup>-2</sup> are then performed to estimate the mean force. Each restrained MD simulation is 100 ps long for both systems. The CV values are recorded every 0.1 ps along the restrained MD trajectories to estimate the mean forces. The uncertainty levels of the reinforced dynamics are set to  $e_0 = 2.0$  kJ mol<sup>-1</sup> rad<sup>-1</sup>,  $e_1 = 3.0$  kJ mol<sup>-1</sup> rad<sup>-1</sup> and  $e_{\text{accept}} = 2.0$  kJ mol<sup>-1</sup> rad<sup>-1</sup>. For RiD, the uncertainty levels  $e_0$  and  $e_1$  remain fixed, but for adaptive RiD they are adaptively changed based on the number of clusters,  $N_c = 13$ . The DNN models contain four hidden layers of size (M1, M2, M3, M4) = (200, 200, 200, 200). Model training is carried out using the deep learning framework TensorFlow<sup>57</sup> with the Adam stochastic gradient descent algorithm<sup>58</sup> with a batch size of  $|B| = 128$ . The learning rate is 0.0006 in the beginning and decays exponentially according to  $\eta(t) = \eta(0) \times d_t^{d_r}$ , where  $t$  is the training step,  $d_r = 0.96$  is the decay rate and  $d_r = 50 \times |D|/|B|$  is the decay step. The total number of training steps is 12,000 ×  $|D|/|B|$ . Four DNN models with independent random initialization are trained in the same way to compute the uncertainty indicator. Details about the hyper-parameter tuning are provided in the final section of the Methods. The whole procedure is conducted for 51 iterations.

For REMD simulations, a total of 20 different temperatures ranging from 300 to 430 K are generated using the temperature generator for REMD simulations<sup>59</sup>. The exchange time between two adjacent replicas is 2 ps and each replica lasts for 100 ns, giving 2 μs of simulation in total. The average acceptance ratio is ~44%. The free energy curve of each angle is calculated from the trajectory at 300 K and the convergence is assessed in Supplementary Fig. 2.

**REMD simulations of peptoid.** The REMD method runs an ensemble of MD simulations at a set of temperatures starting at the investigated temperature and ending at a high temperature that encourages exploration in the conformation space. Intermediate temperatures are provided in the temperature range to make sure that the exchange probability between the replicas running at neighboring temperatures is large enough. A priori knowledge of the FES is thus needed to properly set the highest temperature, which should be high enough to overcome the highest barrier of the free energy landscape and be as low as possible to reduce the number of replicas to save computational costs. In the case of the peptoid trimer, in which a priori knowledge is not available, a systematic of the free energy convergence with the temperature setting is needed.

We report REMD simulations for temperature ranges of 300–430 K, 300–560 K and 300–680 K. Wider temperature ranges are not shown because they need a smaller time step to stabilize the MD simulation at higher-temperature replicas and thus require substantially more computational resources. The free energy curves derived from REMD with the temperature range 300–680 K are the closest to adaptive RiD simulation among these conditions (Supplementary Fig. 7, red lines and gray dashed lines). The shape of the free energies obtained from REMD 300–430 K simulations deviates from those from REMD 300–560 K and 300–680 K, especially the free energies against angles  $\phi_1$ ,  $\phi_2$  and  $\psi_2$  (Supplementary Fig. 7, blue lines). The time series of the peptoid trimer dihedral angles calculated on the continuous replicas spanning different temperatures are shown in Supplementary Fig. 8. In addition, the total numbers of transitions of the six torsion angles  $\omega_1$ ,  $\omega_2$ ,  $\omega_3$ ,  $\phi_1$ ,  $\phi_2$  and  $\phi_3$  of (s1pe)<sub>3</sub> in different REMD simulations are presented in Supplementary Table 2. We observe that there are tens of transitions in the REMD simulations of 300–430 K and many more transitions are seen in the REMD simulations of 300–560 K and 300–680 K, indicating that higher temperatures make it easier for the algorithm to converge. Therefore, overall, a minimal temperature range of 300–560 K is needed. Even with the temperature range 300–680 K, the transition states of the  $\omega$  and  $\phi$  angles are not properly sampled by REMD, so the free energy profile is hard to converge at the transition states. There are two

difficulties in the REMD simulations: (1) a systematic and expensive investigation about the temperature ladder is needed to ensure the convergence of the free energy calculation and (2) the free energies at the transition states of high energy barriers are not available. These difficulties can be avoided by using adaptive RiD.

**Peptoid trimer.** For the peptoid trimer, the molecules are solvated in 3.5 nm × 3.5 nm × 3.5 nm dodecahedron boxes with 973 water molecules. The final systems contain 3,003 atoms. Here the adaptive RiD simulation is conducted for 12 walkers and 140 iterations. All other parameters are the same as for the peptoid, except that the biased MD simulation lasts for 2 ns.

For REMD simulations, a total of 27, 42 and 56 temperature ranges of 300–430 K, 300–560 K and 300–680 K, respectively, are generated using the temperature generator for REMD simulations<sup>59</sup>. The exchange time between two adjacent replicas is 2 ps and each replica lasts for 100 ns, giving 2.7, 4.2 and 5.6 μs of simulations in total, respectively. Three independent REMD simulations of 300–680 K are conducted to obtain the error bars (Supplementary Fig. 6, red lines). The average acceptance ratios are all ~40%.

An additional REMD for each replica, simulated for 400 ns at 300–680 K, is conducted to quantitatively compare the accuracy of the FES calculation using different methods (Supplementary Fig. 4).

For BEMetaD simulations, nine dihedral angles are used as CVs. Nine replicas are used and one for each collective variable. Each replica lasts for 200 ns and the replicas are allowed to exchange every 20 ps. The average acceptance ratio is ~20%. Three different sets of parameters are used. For BE0.2, which is derived from plumID:19.059, the parameters are [PACE=1000 Height=0.2 SIGMA=0.17 GRID\_MIN=-pi GRID\_MAX=pi BIASFACTOR=10.0 TEMP=300]. The parameters of BE0.5 derived from plumID:21.014 are [PACE=500 Height=0.5 SIGMA=0.015 SIGMA\_MAX=0.6 SIGMA\_MIN=0.03 ADAPTIVE=GEOM GRID\_MIN=-pi GRID\_MAX=pi BIASFACTOR=10.0 TEMP=300]. The parameters of BE0.8 are [PACE=500 Height=0.8 SIGMA=0.25 GRID\_MIN=-pi GRID\_MAX=pi BIASFACTOR=10.0 TEMP=300]. The free energy curve of each angle is calculated from the trajectories and convergence is assessed in Supplementary Fig. 3.

For PBMetaD simulations, nine dihedral angles are used as CVs. Nine replicas are simulated and each replica lasts for 200 ns. The parameters are derived from Plumbed Nest with ID plumID:21.014 [PACE=500 Height=0.5 SIGMA=0.015 SIGMA\_MAX=0.6 SIGMA\_MIN=0.03 ADAPTIVE=GEOM GRID\_MIN=-pi GRID\_MAX=pi BIASFACTOR=10.0 TEMP=300]. This PBMetaD setting is denoted by PB0.5.

**Chignolin.** For chignolin, the crystal structure was first obtained from the Protein Data Bank (PDB 5AWL)<sup>35</sup>. To achieve the initial unfolded conformations, one MD simulation in vacuum at 1,000 K is conducted for 5 ns. Twelve fully extended conformations are randomly chosen for the initial conformations of adaptive RiD. They are solvated in a 4.2 nm × 4.2 nm × 4.2 nm dodecahedron box with 1,622 water molecules and two sodium ions to neutralize the charge. All simulations are carried out with the CHARMM22\* force field<sup>60</sup> and the TIP3P water model<sup>56</sup>. The temperature is maintained at 340 K (in agreement with previous works<sup>22,36</sup>). Eighteen backbone dihedral angles are set as CVs. Twelve walkers with different conformations of adaptive RiD are conducted for 31 iterations and the biased MD simulation lasted for 5 ns in each iteration. The CV values are computed every 5 ps. All other parameters are the same as for the peptoid. The reference structure of chignolin is generated from a short, conventional MD simulation starting from the X-ray structure (PDB 5AWL). This reference structure is a better reflection of the actual folded state of the protein in the CHARMM22\* force field than the crystal structure. Given that the maximum r.m.s.d. between the X-ray and NMR (PDB 2RVD) structures is ~0.18 nm, we define the folded state to be the structure with r.m.s.d. < 0.19 nm from the reference structure, and the unfolded state to be the structure with r.m.s.d. > 0.3 nm (ref.<sup>61</sup>). The r.m.s.d. is smoothed along the trajectories with a sliding window of width 3 ns to eliminate overestimation of the folding/unfolding rate due to thermal fluctuations.

For BEMetaD and PBMetaD simulations, 18 backbone dihedral angles are used as CVs. Eighteen replicas are used and each replica lasts for 120 ns. Other parameters are the same as for the peptoid trimer.

**Protein structure refinement.** For protein structure refinement, the initial structures of the targets R0974s1, R0986s1 and R1002-D2 were obtained from the refinement category of the CASP13 competition. They are solvated in 5.5 nm × 5.5 nm × 5.5 nm, 5.8 nm × 5.8 nm × 5.8 nm and 5.4 nm × 5.4 nm dodecahedron boxes with 3,384, 4,191 and 3,334 water molecules, respectively. Ions are added to neutralize the charge. All simulations are carried out with the CHARMM36m force field<sup>62</sup> and the TIP3P water model<sup>56</sup>. The temperature is maintained at 300 K. A total of 136, 182 and 116 backbone dihedral angles are set as CVs. Eight walkers are used and the biased MD simulation lasts for 6 ns in each iteration. The CV values are computed every 6 ps. All other parameters are the same as for the peptoid except that the widths of the hidden layers are chosen as (M1, M2, M3, M4) = (1,200, 1,200, 1,200, 1,200) for the DNN models. The flat-bottom harmonic restraint potential applied to each C $\alpha$  atom is defined as

$$V_{\text{fb}}(r_i) = \frac{1}{2} k_{\text{fb}} [d_g(r_i; R_i) - r_{\text{fb}}]^2 H[d_g(r_i; R_i) - r_{\text{fb}}], \quad (3)$$



where  $R_i$  denotes the reference position of the  $i$ th Co $\alpha$  atom,  $r_{ib}$  is the distance from the center with a flat potential,  $k_b$  denotes the force constant,  $H$  denotes the Heaviside function and  $d_b(r_i; R_i)$  is the distance from the reference position. Here we set  $r_{ib}$  to 0.6 nm and  $k_b$  to 12 kJ mol<sup>-1</sup> nm<sup>-2</sup>.

**MCMC simulations.** We notice that the FES is a logarithm of the probability distribution, that is

$$A(s) = -k_b T \ln p(s) \quad (4)$$

so the low-dimensional FES is computed from the marginal distribution of the high-dimensional probability distribution corresponding to the high-dimensional FES. In this work, we use the MCMC method to calculate the marginal distribution.

For example, we have an  $M$ -dimensional CV space  $s = (s_1, \dots, s_M)$  and want to calculate the FES  $A(s_1)$  from  $A(s_1, \dots, s_M)$ . Since we have the definition for the marginal distribution on  $s_1$

$$p(s_1) = \int p(s_1, \dots, s_M) ds_2 \dots ds_M \quad (5)$$

then the FES on  $s_1$  is given by

$$A(s_1) = -k_b T \ln \int e^{-\frac{1}{k_b T} A(s_1, \dots, s_M)} ds_2 \dots ds_M. \quad (6)$$

The integration in equation (5) or (6) is computed by MCMC. Here, we carry out 2,000 independent MC samplers and each lasts 10<sup>6</sup> steps. The example can be easily generalized to any FES defined on a low-dimensional subspace of the high-dimensional CV space.

Note that the MCMC sampling is performed on the FES, so it is very efficient. The convergence of the MCMC simulations is assessed in Supplementary Fig. 5.

**A guideline for tuning the hyper-parameters of the adaptive RiD.** In the hyper-parameter tuning procedure, we first estimate the statistical error introduced by the restrained MD simulations. This error defines the highest accuracy achievable by our DNN representation. The hyper-parameters, such as batch size, start learning rate and learning rate decay speed, are then tuned to minimize the number of epochs needed to achieve the optimal accuracy. In the first few adaptive RiD iterations, the width of the DNN may be chosen to be a relatively small value, for example, 100 for each hidden layer. As the adaptive RiD proceeds, more parts of the FES are explored and the training data accumulate, and the accuracy of the DNN model is observed to decrease. This indicates that the current DNN architecture is not powerful enough compared with the complexity of the explored FES. We stop the adaptive RiD manually when the relative error reaches ~0.5, enlarge the DNN with a sub-network initialized by the original DNN, and then retrain the new DNN. This can substantially reduce the error of the DNN and the adaptive RiD can continue. It is noted that the strategy of gradually enlarging the DNN helps to determine its size, but is not necessary, because using a large enough DNN at the beginning would not cause any difficulty in training the DNN.

## Data availability

The initial files of all examples for running adaptive RiD are available from Zenodo<sup>63</sup>. Our peptoid models come from Weiser's work<sup>32</sup>. Our chignolin model is obtained from the Protein Data Bank (PDB 5AWL). The MD trajectories of chignolin from Anton can be obtained from ref. <sup>36</sup>. The targets in CASP13 can be obtained from the official CASP list (<https://predictioncenter.org/casp13/targetlist.cgi>). The Markov state models of R0974s1, R0986s1 and R1002-D2 can be obtained from the work of Heo and colleagues<sup>47</sup>. The input PLUMED2 files are available via Plumed Nest under plumid:21.034. Source data are provided with this paper.

## Code availability

Python implementations of our codes are available at GitHub (<https://github.com/dongdawn/rid>) and Zenodo<sup>64</sup>.

Received: 4 April 2021; Accepted: 15 November 2021;

Published online: 24 December 2021

## References

1. Laio, A. & Parrinello, M. Escaping free-energy minima. *Proc. Natl Acad. Sci. USA* **99**, 12562–12566 (2002).
2. Barducci, A., Bussi, G. & Parrinello, M. Well-tempered metadynamics: a smoothly converging and tunable free-energy method. *Phys. Rev. Lett.* **100**, 020603 (2008).
3. Torrie, G. M. & Valleau, J. P. Nonphysical sampling distributions in Monte Carlo free-energy estimation: umbrella sampling. *J. Comput. Phys.* **23**, 187–199 (1977).
4. Rosso, L., Mináry, P., Zhu, Z. & Tuckerman, M. E. On the use of the adiabatic molecular dynamics technique in the calculation of free energy profiles. *J. Chem. Phys.* **116**, 4389–4402 (2002).
5. Maragliano, L. & Vanden-Eijnden, E. A temperature accelerated method for sampling free energy and determining reaction pathways in rare events simulations. *Chem. Phys. Lett.* **426**, 168–175 (2006).
6. Abrams, J. B. & Tuckerman, M. E. Efficient and direct generation of multidimensional free energy surfaces via adiabatic dynamics without coordinate transformations. *J. Phys. Chem. B* **112**, 15742–15757 (2008).
7. Abrams, C. F. & Vanden-Eijnden, E. Large-scale conformational sampling of proteins using temperature-accelerated molecular dynamics. *Proc. Natl Acad. Sci. USA* **107**, 4961–4966 (2010).
8. Maragliano, L. & Vanden-Eijnden, E. Single-sweep methods for free energy calculations. *J. Chem. Phys.* **128**, 184110 (2008).
9. Piana, S. & Laio, A. A bias-exchange approach to protein folding. *J. Phys. Chem. B* **111**, 4553–4559 (2007).
10. Pfäendtner, J. & Bonomi, M. Efficient sampling of high-dimensional free-energy landscapes with parallel bias metadynamics. *J. Chem. Theory Comput.* **11**, 5062–5067 (2015).
11. Arushi, P., Fu, C. D., Massimiliano, B. & Jim, P. Biasing smarter, not harder, by partitioning collective variables into families in parallel bias metadynamics. *J. Chem. Theory Comput.* **14**, 4985–4990 (2018).
12. Stecher, T., Bernstein, N. & Csányi, G. Free energy surface reconstruction from umbrella samples using Gaussian process regression. *J. Chem. Theory Comput.* **10**, 4079–4097 (2014).
13. Mones, L., Bernstein, N. & Csányi, G. Exploration, sampling and reconstruction of free energy surfaces with Gaussian process regression. *J. Chem. Theory Comput.* **12**, 5100–5110 (2016).
14. Schneider, E., Dai, L., Topper, R. Q., Drechsel-Grau, C. & Tuckerman, M. E. Stochastic neural network approach for learning high-dimensional free energy surfaces. *Phys. Rev. Lett.* **119**, 150601 (2017).
15. Zhang, L., Wang, H. & E, W. Reinforced dynamics for enhanced sampling in large atomic and molecular systems. *J. Chem. Phys.* **148**, 124113 (2018).
16. Sidky, H. & Whitmer, J. K. Learning free energy landscapes using artificial neural networks. *J. Chem. Phys.* **148**, 104111 (2018).
17. Guo, A. Z. et al. Adaptive enhanced sampling by force-biasing using neural networks. *J. Chem. Phys.* **148**, 134108 (2018).
18. Sultan, M. M., Waymunt-Steele, H. K. & Pande, V. S. Transferable neural networks for enhanced sampling of protein dynamics. *J. Chem. Theory Comput.* **14**, 1887–1894 (2018).
19. Bonati, L., Zhang, Y.-Y. & Parrinello, M. Neural networks-based variationally enhanced sampling. *Proc. Natl Acad. Sci. USA* **116**, 17641–17647 (2019).
20. Sevgen, E., Guo, A., Sidky, H., Whitmer, J. K. & de Pablo, J. J. Combined force-frequency sampling for simulation of systems having rugged free energy landscapes. *J. Chem. Theory Comput.* **16**, 1448–1455 (2020).
21. Valsson, O. & Parrinello, M. Variational approach to enhanced sampling and free energy calculations. *Phys. Rev. Lett.* **113**, 090601 (2014).
22. Shaffer, P., Valsson, O. & Parrinello, M. Enhanced, targeted sampling of high-dimensional free-energy landscapes using variationally enhanced sampling, with an application to chignolin. *Proc. Natl Acad. Sci. USA* **113**, 1150–1155 (2016).
23. Cendagorta, J. R., Tolpin, J., Schneider, E., Topper, R. Q. & Tuckerman, M. E. Comparison of the performance of machine learning models in representing high-dimensional free energy surfaces and generating observables. *J. Phys. Chem. B* **124**, 3647–3660 (2020).
24. Sugita, Y. & Okamoto, Y. Replica-exchange molecular dynamics method for protein folding. *Chem. Phys. Lett.* **314**, 141–151 (1999).
25. Ducheyne, P. *Comprehensive Biomaterials* Vol. 1 (Elsevier, 2015).
26. Sun, J. & Zuckermann, R. N. Peptoid polymers: a highly designable bioinspired material. *ACS Nano* **7**, 4715–4732 (2013).
27. Mojsoska, B., Zuckermann, R. N. & Jenssen, H. Structure–activity relationship study of novel peptoids that mimic the structure of antimicrobial peptides. *Antimicrob. Agents Chemother.* **59**, 4112–4120 (2015).
28. Li, N. et al. Blockade of CD28 by a synthetic peptoid inhibits T-cell proliferation and attenuates graft-versus-host disease. *Cell. Mol. Immunol.* **7**, 133–142 (2010).
29. Luo, Y. et al. Aβ42-binding peptoids as amyloid aggregation inhibitors and detection ligands. *ACS Chem. Neurosci.* **4**, 952–962 (2013).
30. Mirijanian, D. T., Mannige, R. V., Zuckermann, R. N. & Whitelam, S. Development and use of an atomistic CHARMM-based forcefield for peptoid simulation. *J. Comput. Chem.* **35**, 360–370 (2014).
31. Mukherjee, S., Zhou, G., Michel, C. & Voelz, V. A. Insights into peptoid helix folding cooperativity from an improved backbone potential. *J. Phys. Chem. B* **119**, 15407–15417 (2015).
32. Weiser, L. J. & Santiso, E. E. Molecular modeling studies of peptoid polymers. *AIMS Mater. Sci.* **4**, 1029–1051 (2017).
33. Weiser, L. J. & Santiso, E. E. A CGenFF-based force field for simulations of peptoids with both *cis* and *trans* peptide bonds. *J. Comput. Chem.* **40**, 1946–1956 (2019).

34. Gorske, B. C., Stringer, J. R., Bastian, B. L., Fowler, S. A. & Blackwell, H. E. New strategies for the design of folded peptoids revealed by a survey of noncovalent interactions in model systems. *J. Am. Chem. Soc.* **131**, 16555–16567 (2009).
35. Honda, S. et al. Crystal structure of a ten-amino acid protein. *J. Am. Chem. Soc.* **130**, 15327–15331 (2008).
36. Lindorff-Larsen, K., Piana, S., Dror, R. O. & Shaw, D. E. How fast-folding proteins fold. *Science* **334**, 517–520 (2011).
37. Kùhrová, P., De Simone, A., Otyepka, M. & Best, R. B. Force-field dependence of chignolin folding and misfolding: comparison with experiment and redesign. *Biophys. J.* **102**, 1897–1906 (2012).
38. Zhang, T., Nguyen, P. H., Nasica-Labouze, J., Mu, Y. & Derreumaux, P. Folding atomistic proteins in explicit solvent using simulated tempering. *J. Phys. Chem. B* **119**, 6941–6951 (2015).
39. Miao, Y., Feixas, F., Eun, C. & McCammon, J. A. Accelerated molecular dynamics simulations of protein folding. *J. Comput. Chem.* **36**, 1536–1549 (2015).
40. Jumper, J. et al. Highly accurate protein structure prediction with AlphaFold. *Nature* **596**, 583–589 (2021).
41. Zemla, A. LGA: a method for finding 3D similarities in protein structures. *Nucleic Acids Res.* **31**, 3370–3374 (2003).
42. Raval, A., Piana, S., Eastwood, M. P., Dror, R. O. & Shaw, D. E. Refinement of protein structure homology models via long, all-atom molecular dynamics simulations. *Proteins* **80**, 2071–2079 (2012).
43. Feig, M. & Mirjalili, V. Protein structure refinement via molecular-dynamics simulations: what works and what does not? *Proteins* **84**, 282–292 (2016).
44. Heo, L. & Feig, M. Experimental accuracy in protein structure refinement via molecular dynamics simulations. *Proc. Natl Acad. Sci. USA* **115**, 13276–13281 (2018).
45. Park, H., Ovchinnikov, S., Kim, D. E., DiMaio, F. & Baker, D. Protein homology model refinement by large-scale energy optimization. *Proc. Natl Acad. Sci. USA* **115**, 3054–3059 (2018).
46. Park, H. et al. High-accuracy refinement using Rosetta in CASP13. *Proteins* **87**, 1276–1282 (2019).
47. Heo, L., Arbour, C. F. & Feig, M. Driven to near-experimental accuracy by refinement via molecular dynamics simulations. *Proteins* **87**, 1263–1275 (2019).
48. Zhang, J. & Zhang, Y. A novel side-chain orientation dependent potential derived from random-walk reference state for protein fold selection and structure prediction. *PLoS ONE* **5**, e15386 (2010).
49. Jing, X. & Xu, J. Improved protein model quality assessment by integrating sequential and pairwise features using deep learning. *Bioinformatics* **36**, 5361–5367 (2020).
50. Abraham, M. J. et al. GROMACS: high performance molecular simulations through multi-level parallelism from laptops to supercomputers. *SoftwareX* **1**, 19–25 (2015).
51. Tribello, G. A., Bonomi, M., Branduardi, D., Camilloni, C. & Bussi, G. PLUMED 2: new feathers for an old bird. *Comput. Phys. Commun.* **185**, 604–613 (2014).
52. Bussi, G., Donadio, D. & Parrinello, M. Canonical sampling through velocity rescaling. *J. Chem. Phys.* **126**, 014101 (2007).
53. Parrinello, M. & Rahman, A. Polymorphic transitions in single crystals: a new molecular dynamics method. *J. Appl. Phys.* **52**, 7182 (1981).
54. Darden, T., York, D. & Pedersen, L. Particle mesh Ewald: an  $N\log(N)$  method for Ewald sums in large systems. *J. Chem. Phys.* **98**, 10089–10092 (1993).
55. Hess, B., Bekker, H., Berendsen, H. & Fraaije, J. LINCS: a linear constraint solver for molecular simulations. *J. Comput. Chem.* **18**, 1463–1472 (1997).
56. Jorgensen, W. L., Chandrasekhar, J., Madura, J. D., Impey, R. W. & Klein, M. L. Comparison of simple potential functions for simulating liquid water. *J. Chem. Phys.* **79**, 926–935 (1983).
57. Abadi, M. et al. Tensorflow: a system for large-scale machine learning. In *Proc. 12th USENIX Conference on Operating Systems Design and Implementation OSDI'16* 265–283 (USENIX Association, 2016).
58. Kingma, D. & Ba, J. Adam: a method for stochastic optimization. In *Proc. 3rd International Conference on Learning Representations (ICLR)*, 2015).
59. Patriksson, A. & van der Spoel, D. A temperature predictor for parallel tempering simulations. *Phys. Chem. Chem. Phys.* **10**, 2073–2077 (2008).
60. Piana, S., Lindorff-Larsen, K. & Shaw, D. E. How robust are protein folding simulations with respect to force field parameterization? *Biophys. J.* **100**, L47–L49 (2011).
61. Paissoni, C. & Camilloni, C. How to determine accurate conformational ensembles by metadynamics metainference: a chignolin study case. *Front. Mol. Biosci.* **8**, 694130 (2021).
62. Huang, J. et al. CHARMM36m: an improved force field for folded and intrinsically disordered proteins. *Nat. Methods* **14**, 71–73 (2017).
63. Wang, D. & Wang, Y. Initial files of examples for running adaptive RiD. *Zenodo* <https://doi.org/10.5281/zenodo.5674402> (2021).
64. Wang, D. & Wang, Y. Codes of adaptive reinforced dynamics. *Zenodo* <https://doi.org/10.5281/zenodo.5674474> (2021).

## Acknowledgements

The work of D.W., L.Z. and W.E. is supported in part by a gift from iFlytek to Princeton University. The work of H.W. is supported by the National Science Foundation of China under grant no.11871110 and Beijing Academy of Artificial Intelligence (BAAI). The work of L.Z. is also supported by the DOE Center of Chemistry in Solutions and at Interfaces (CSI) through award no. DE-SC0019394.

## Author contributions

D.W., L.Z., H.W. and W.E. conceptualized the research. D.W., Y.W. and J.C. conducted the research and performed data analysis. D.W., L.Z., H.W. and W.E. drafted the manuscript. All authors commented on and revised the manuscript.

## Competing interests

The authors declare no competing interests.

## Additional information

**Supplementary information** The online version contains supplementary material available at <https://doi.org/10.1038/s43588-021-00173-1>.

**Correspondence and requests for materials** should be addressed to Linfeng Zhang or Han Wang.

**Peer review information** *Nature Computational Science* thanks Wojtech Spiwok, Max Bonomi and the other, anonymous, reviewer(s) for their contribution to the peer review of this work. Handling editor: Jie Pan, in collaboration with the *Nature Computational Science* team.

**Reprints and permissions information** is available at [www.nature.com/reprints](http://www.nature.com/reprints).

**Publisher's note** Springer Nature remains neutral with regard to jurisdictional claims in published maps and institutional affiliations.

© The Author(s), under exclusive licence to Springer Nature America, Inc. 2021